University of Huddersfield Repository

Stetsyuk, V., Soulopoulos, N., Hardalupas, Y. and Taylor, A. M. K. P.

Rayleigh scattering temperature measurements in a swirl stabilized burner

Original Citation

Stetsyuk, V., Soulopoulos, N., Hardalupas, Y. and Taylor, A. M. K. P. (2013) Rayleigh scattering temperature measurements in a swirl stabilized burner. In: European Combustion Meeting 2013, 25th - 28th June 2013, Lund University, Sweden.

This version is available at http://eprints.hud.ac.uk/27902/

Rayleigh scattering temperature measurements in a swirl stabilized burner

V. Stetsyuk[*1], N. Soulopoulos[1], Y. Hardalupas[1] and Alex M. K. P. Taylor[1]

[1] Imperial College London, Department of Mechanical Engineering,
South Kensington Campus, London, UK

Abstract
Rayleigh scattering temperature measurements were obtained in a turbulent reactive swirling coaxial jet discharged from a swirl-stabilized burner along the jet-flame centerline. They are reported up to 10 fuel nozzle diameters downstream of the burner exit at a Reynolds number of 29000. The effect of swirl numbers (S=0.3, 0.58, 1.07) on the temperature fields, the power spectral density of temperature fluctuations and on the probability density functions of the temperature fluctuations was determined.

1. Introduction

In diffusion flames the combustion process is typically governed by the mixing time because the chemical reaction timescale is very short of the order of 2-5 ms. The mixing time is directly proportional to the turbulence kinetic energy and the energy dissipation rate. The process of mixing and combustion takes place simultaneously at small scales of flow. In order to increase mixing and sustain stable combustion, the flame is anchored by a recirculation zone, which is formed in swirling flows. Axial, radial and tangential velocity components create corresponding pressure gradients and a region of low pressure is generated within the central core of the swirling jet. At a certain degree of swirl the momentum of rotating fluid can no longer overcome the pressure gradient, created by the swirling components, leading to flow reversal and vortex breakdown. This flow reversal zone, which is on average appears as a flow recirculation zone, is the primary source of flame stabilization, due to recirculation of hot gases (burnt products), mixing with the fresh reactants and subsequent ignition. The central flow zone experiencing solid body rotation is typically defined as the vortex core.

The swirling flow can be seen as a combination of a free vortex, in which the tangential velocity is inversely proportional to the radius and a forced vortex in which the tangential velocity is proportional to the radius. A commonly used parameter that describes swirling flows is the swirl number, which is defined as the ratio of the axial flux of angular momentum to the axial flux of axial momentum multiplied with the equivalent exit radius [1] (D is the burner exit diameter):

$$S = \frac{2G_\theta}{G_z D} \qquad [1]$$

$$G_\theta = 2\pi\rho \int_{r=r_i}^{R} UW_r r dr \qquad [2]$$

$$G_z = 2\pi\rho \int_{r=r_i}^{R} UU r dr \qquad [3]$$

All swirling flows can generally be split into two groups, i.e. weak S<0.6 and strong S>0.6 swirling flows. For low swirl numbers, S<0.6, the flow patterns demonstrate so-called a 'solid body' rotation, which is initially observed at approximately S=0.1. For high swirl numbers, S>0.6, flow develops a structure with rapidly rotating core, which is surrounded by an annulus of low vorticity. A flow reversal is observed in the central region of the swirling flow [2]. In this work, both weak and strong swirling flows are studied with the maximum swirl number of 1.07. Even though weak swirling flows have limited industrial applicability, it is necessary to investigate such regimes and compare with highly swirled flows. The effect of the vortex breakdown is still not well understood and also requires careful attention. The detailed description of the characteristics of the swirling flows and associated effects such as vortex breakdown phenomenon and flame stabilization can be found, for example, in references [3, 4, 5 and 6].

2. Motivation and objectives

The background motive of the present work originates from combustion in gas turbine and jet engines with emphasis on the reduction of nitrogen oxides from current and prospective combustion systems. The present work also aims to provide experimental data, which can be used to evaluate existing and prospective combustion models. Despite considerable research, the temperature statistics are virtually not available in reacting swirling flows. The temperature measurements in reacting flows are, therefore, considered to be one of many problems that need to be addressed. This work presents experimental studies of temperature measurements in swirling flows with a variable degree of swirl at a constant Reynolds number in coflow air jet of 29000. The scalar mixing in

non-reacting swirling coaxial jets discharged from the same swirl burner is also discussed in [7].

The remaining paper is structured as follows. Section 3 describes the swirling air flow burner and the optical instrumentation used to measure the Rayleigh scattering light intensity, which is then converted to the temperature according to the explanation provided in Section 4, which describes the Rayleigh thermometry. Finally, Section 5 describes the results and discusses the findings. The paper ends with a summary of the main conclusions.

3. Experimental setup

The burner used in this study is shown in Figure 1 and was based on [8] and replicated in [9]. The burner comprised two concentric pipes with the annulus supplying air and the central pipe delivering gaseous fuel. The central pipe had an inner diameter D_f of 15 mm and an outer diameter of 18 mm, was 0.75 m long and was located concentrically in the outer pipe of inner diameter, D, 50.8 mm and length downstream of the swirl chamber of 264 mm. The annular air stream was divided into two separately metered streams. One ('tangential air') passed through a static Swirler containing six tangential slots to impart angular momentum. The static Swirler was located in a plenum chamber in which the Swirling air was combined with the second stream, which delivered 'axial air'. Metal plates were installed in the axial and tangential air sections of the plenum chamber to ensure that the axial and tangential air streams were distributed uniformly upstream of the inlets into the annular air supply stream of the burner, where they were combined to control the strength of Swirl at the burner exit. The tangential and axial air flowrates were metered by flowmeters after correction to atmospheric pressure and temperature. The axial direction, parallel to the flow propagation, was denoted as 'y' and the radial direction, perpendicular to the main direction of the flow, as 'x'. The swirl number of the coflow was calculated in [9] by using measured axial and tangential velocity profiles with a laser Doppler anemometer at y/D=0.04. Reynolds number in the fuel pipe was computed to be 2134 based on the bulk velocity of 6.19 (m/s). Reynolds number in the coflow air jet was computed to be 28662 based on the bulk velocity of 8.46 (m/s).

The optical setup consisted of a laser, sheet forming optics, a CCD camera and associated control devices. A class-IV high power pulsed neodymium-doped yttrium aluminium garnet (Nd:YAG) frequency doubled Q-switched laser (Quanta-Ray PRO-Series, PRO-270-10) from Spectra-Physics Inc. was used emitting in the green visible range of 532 nm. The laser beam was produced at the fundamental wavelength of 1064 nm and passed through a frequency doubler to produce 532 nm. The laser pulse width was in the range of 8-12 ns at Full Width at Half Maximum at 1064 nm and 1-2 ns at 532 nm. The laser was controlled locally by using the standard table-top controller for alignment purposes and electronically from a computer during the

experiments. The sheet forming optic consisted of a single mirror with diameter of 25.4 mm and a cylindrical positive lens with focal length of f-310 mm. The lens was used to focus the laser beam into a thin waist, with focal point located at the axis of symmetry of the flow. The average laser energy at the exit port of the laser was circa 950 mJ/pulse. Actual laser energy fluctuations during experiments from pulse to pulse were less than ± 2.7%. The laser beam waist from the laser was measured directly by using the CCD camera technique. The positive cylindrical lens was rotated to 90^0, so the laser sheet waist thickness could be captured by measuring the Rayleigh scattering intensity from the air. Averaging CCD images was done in order to remove image noise, laser beam intensity fluctuations and eliminate effects of Mie scattering from dust particles.
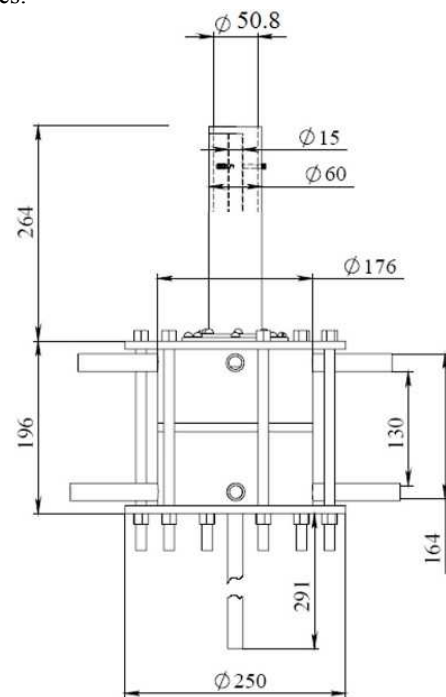

Figure 1: Atmospheric burner used for temperature measurements.

The beam waist was defined as equal to the distance between the two points on the intensity distribution that are $1/e^2$ (0.135 times the maximum value) and was defined to be 0.4 mm. A double frame CCD camera from LaVision Inc. was used in this work. The camera was equipped with a Nikon lens with focal length f=50 mm and f1.2 (where f-is the aperture 'f' number). A 13 mm extension ring was also used after the camera lens for tighter focusing. A 532-3 bandpass filter was used in the front of the camera lens in order to block any incoming light that might interfere with the acquired signal. The magnification (nominal resolution) was determined by using a special calibration target plate and was found to be 0.025 mm/pixel. The camera exposure time was set to be 1 μs at the maximum aperture of 1.2. The synchronization of the laser flashlamp and the CCD camera was achieved by using a programmable PC-based timing unit using TTL pulses.

The laser flashlamp was triggered every time when an image was obtained. The Q-switch delay was set by a top-table controller to its optimal value in order to deliver maximum power, which was monitored by a laser power meter.
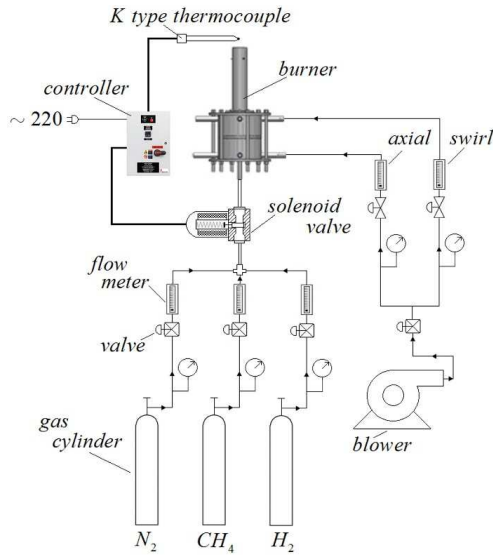

Figure 2: Schematic representation of rotameter feeds.
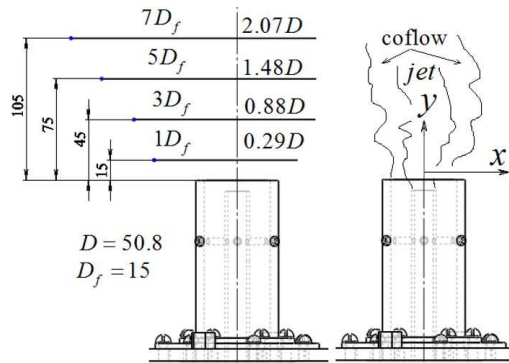

Figure 3: A schematic view of laser sheet positions during measurements. Laser sheet positions are shown in absolute values (mm), normalized by the fuel pipe internal diameter D_f and by the burner diameter D.

3. Rayleigh thermometry

Rayleigh thermometry is based on the Rayleigh scattering. It is the elastic scattering of light or other electromagnetic radiation from atoms, molecules or particles that are smaller than the wavelength of the light. The elastic scattering of light by a molecule or a particle is proportional to their Rayleigh scattering cross section, which is an intrinsic property of a molecule. The Rayleigh scattering is commonly assumed to be temperature-independent. The wavelength of scattered light is unchanged (elastic scattering) and the scattering amplitude is proportional to the weighted sum of the number of scatters in the observation volume. The scattering intensity is also proportional to a wavelength of light and thus at 450 nm in the blue spectrum is

scattered a factor 6 times as efficient as a wavelength of 650 nm in the red.

In order to determine the flame temperature, the ratio of differential cross sections of air/mixture must be known. In turbulent non-premixed flames this ratio is unknown and cannot be determined without additional information from the experimental data. For example, simultaneous Rayleigh/Raman scattering technique can be used to measure mixture composition and the Rayleigh signals [10]. On the other hand, there is also an alternative approach that makes possible direct Rayleigh scattering without having additional information. The idea behind this approach is that any fuel that have constant scattering cross section across the flame eliminates differential cross section dependence. The fuel that was used in this work was occasionally called the DLR fuel and consisted of a mixture with volumetric composition of 22.1% of CH_4, 33.2% of H_2, and 44.7% of N_2 (stoichiometric mixture fraction is 0.167). The ratio of Rayleigh scattering cross section across the flame as a function of mixture fraction was computed and shown in Figure 4. Temperature calibration and validation were done by using a premixed flat burner, which was based on the McKenna burner. If Rayleigh scattering cross section is assumed constant across the flame, the temperature is simply computed as follows [11]:

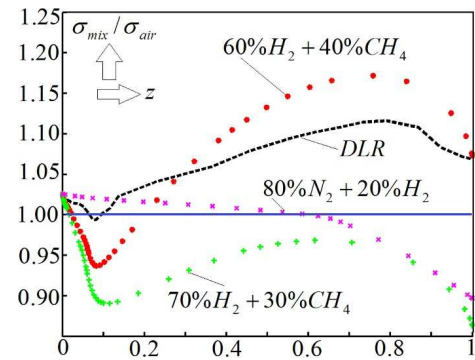$$T = \frac{S_{ref}}{S_{meas}} T_{ref} \qquad [4]$$

Figure 4: Variation of the Rayleigh scattering cross section across the flame computed from opposed jet flow simulation for various fuel compositions.

An initial image processing for the temperature computation involved two steps. The most important issue was the elimination the bright spots (due to overexposed pixels), which were due to Mie scattering from dust particles. The elimination of the bright spots from the raw images was achieved by thresholding, which was the simplest method of image denoising. During the thresholding process, individual pixels in computed temperature images were compared to the threshold value, which was the reference temperature. Finally, the temperature images after processing through

thresholding were filtered by using a median filter with a kernel of 3×3 pixels.

4. Results and discussion

A photograph of flames operating at 0.9 overall equivalence ratio and swirl numbers equal to 0.3, 0.58 and 1.07 is shown in Figure 5 and 6. A thermocouple that is seen in the images was used to detect the flame temperature in order to provide a safety protection from incidental blow-off. The flame was blue-coloured tulip cup shaped for moderate and highest swirl numbers of 0.58 and 1.07, while for the lowest swirl number the flame seemed to have cylindrical shape without significant divergence and resembled a long jet flame. The higher swirl number 0.58 and 1.07 produced wider flame, which could be the representation of positive radial stretch as a result of the large tangential velocity gradients. The positive radial stretch also shortens the flame height and increases the volumetric burning rate due to larger surface area.
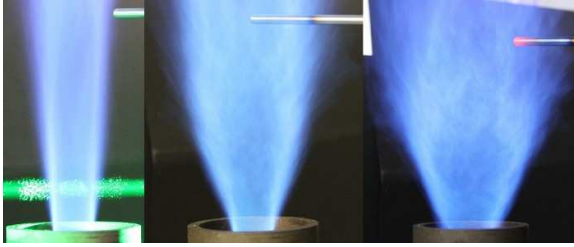

Figure 5: A photograph of the flame (side view) as a function of the swirl number. From left to right S=0.3, 0.58 and 1.07, overall stoichiometric ratio is 0.9. A thermocouple that is seen in the images was used to detect the flame temperature in order to provide a safety protection from incidental blow-off. A position of laser sheet is also shown at y/D_f=1 with clearly visible Mie scattering from the dust particles.

Figure 6: A photograph of the flame (angled view) as a function of swirl number. From left to right S=1.07, 0.58 and 0.3.

Instantaneous temperature fields for S=0.58 are presented in Figure 7 as a function of downstream position. Time averaged temperature fields and temperature standard deviation are also shown in Figures 8 and 9 for the same swirl number. At lower axial downstream positions y/Df=1-3, the temperature is seen as narrow zones of high temperature, which are embedded into cold field. At higher positions, the temperature field becomes more distributed, in which no distinct high temperature zones can be observed. In addition, for lowest swirl number of 0.3 and at lower

axial positions the high temperature zone fluctuates within the shear layer, i.e. ±0.3 x/R.

Centreline temperature at lower axial positions seems to be close to the ambient temperature (or air stream temperature), while at higher positions due to enhanced mixing, the centreline temperature increases. At intermediate swirl number of 0.58 the temperature is more affected by the level of mixing, which is seen as more distributed high temperature zones, especially at lower downstream location. At higher downstream positions, the temperature distribution tends to be more uniform, which is observed even at the instantaneous images. As in case of low swirl number of 0.3, the centreline temperature increases with the distance from the jet origin, or more precisely from the burner exit. The temperature field seems to be nearly homogeneous at the highest downstream positions y/Df=10 for S=1.07 and no significant temperature fluctuations are observable. The centreline temperature expresses the same trend as in previous cases of low and moderate swirl numbers, i.e. gradually increases with the distance from the burner exit.
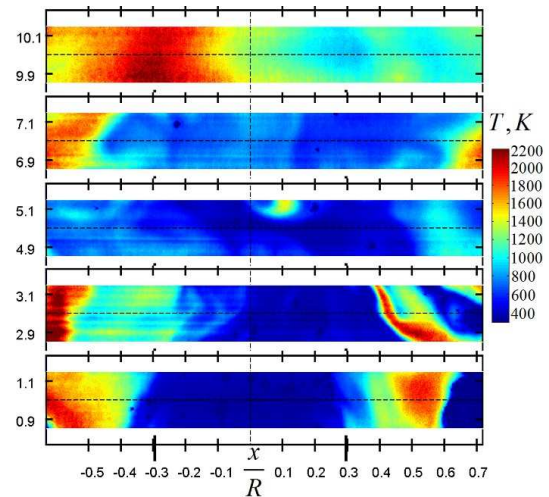

Figure 7: Instantaneous temperature fields (K) for S=0.58 at y/D_f=10, 7, 5, 3, 1 (from top to bottom). The maximum recorded temperature was circa 2200 K.

At low swirl number the temperature standard deviation is highly non-uniform, especially at lower downstream positions, which indicates high temperature fluctuation. In contrast, for intermediate and the highest swirl numbers, the standard deviation becomes smaller and more distributed.

The probability density function (p.d.f.) of the temperature fluctuations was computed from the instantaneous temperature after subtracting the mean and normalizing by the standard deviation of the temperature. The range of the values was divided in a number of equal bins (50 bins were typically used) and the number of occurrences in each bin was counted. The p.d.f. was computed as N/LW, where N is the count of values in each bin or frequency, W is the width of the bin and L is the total number of samples (cardinality of a dataset). The width of the bin was assessed through a

set of trial and error procedures and it was found that the convergence of the p.d.f. was almost independent of the number of bins. Data for each probability function of temperature fluctuations was compiled by considering the local window of axial length of 1.27 mm and radial length of 1.55 mm containing 2976 data points and over 1000 images resulting in circa 3e6 temperature data points for each spatial location. Five spatial locations were investigated.
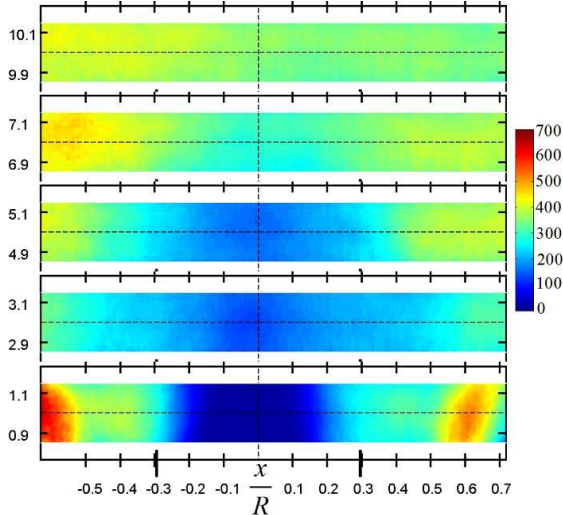

Figure 8: Temperature standard deviation computed from 1000 instantaneous images for S=0.58 at y/D$_f$=10, 7, 5, 3, 1 (from top to bottom).
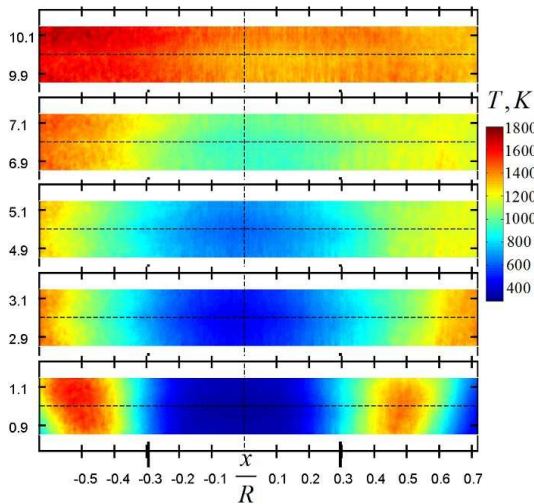

Figure 9: Mean temperature computed from 1000 instantaneous images for S=0.58 at y/Df=10, 7, 5, 3, 1 (from top to bottom).

Measured probability density function of temperature fluctuations at various downstream positions and spatial location in the flow exhibited a wide range of shapes. The wide range of shapes consists of unimodal and bimodal both equal and unequal distributions. Zones with the low temperature fluctuations typically demonstrate unimodal distribution with high kurtosis, while zones with high temperature fluctuations occasionally demonstrate a bimodal distribution. At

larger downstream locations and higher swirl numbers the p.d.fs. were typically unimodal even though not entirely symmetrical. It seems to be plausible to assume a Gaussian distribution for the p.d.f. of the temperature fluctuations for most of the cases. In the cold centreline zone close to the burner exit, the measured p.d.fs. for low swirl number of 0.3 and intermediate 0.58 at y/Df=1 were nearly triangular (example in Figure 11). It can also be said that a bimodal distribution occurs when the output from two processes, each one from the Gaussian distribution with different mean, are mixed. In the case of the temperature fluctuations it can be thought as the two streams of hot and cold fluid, which are locally mixed within the window of interest.
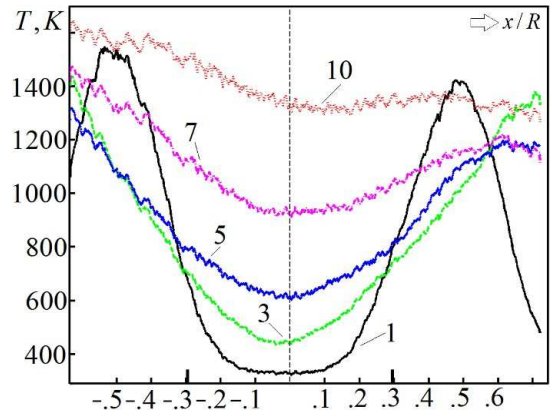

Figure 10: Mean temperature radial profiles for S=0.58 as a function of downstream positions.

Power spectral density of temperature fluctuations was determined as ensemble average from 1000 instantaneous images and computed as the ensemble average of the square of the magnitude of the 2D Fast Fourier Transform of the temperature fluctuations. The power spectrum was normalized by its corresponding maximum. All of the spectra (for all swirl numbers) seem to exhibit a similar appearance, i.e. they are flat at low frequencies, begin to roll off at quite different wavenumbers, decreasing more rapidly in the dissipation range. The temperature spectra shift to lower frequencies with increasing downstream distance, which is clearly seen in Figure 12. This reduction in frequency can be explained by the increase in dissipative length scales due to higher temperature and perhaps lower velocity. Higher temperature at higher downstream positions leads to higher viscosity and as a result to higher viscosity dumping effects. A small inertial subrange, which can be hardly seen at lower axial distances is likely because the turbulence is not fully developed and perhaps due to low local Reynolds number. On the other hand, an extended inertial subrange at higher downstream positions, especially for higher swirl numbers 0.58 and 1.07 is the sign of fully developed turbulence.
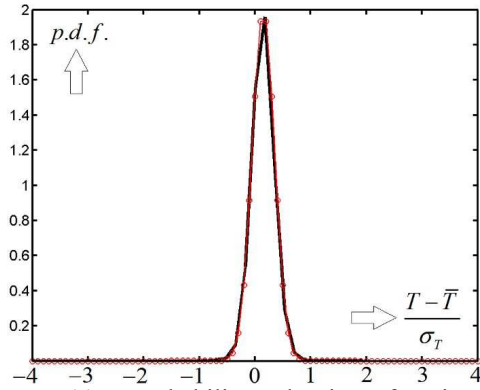
Figure 11: Probability density function of temperature fluctuation computed from centreline. Gaussian distribution is also plotted for comparison.
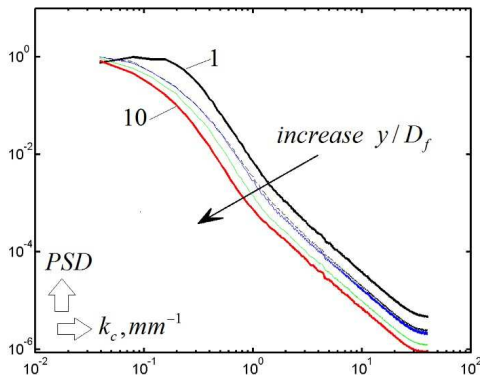

Figure 12: Normalized fluctuating temperature power spectra as a function of downstream distance for S=0.58.

5. Conclusion

Rayleigh scattering temperature measurements were obtained in a turbulent reactive swirling coaxial jet discharged from a swirl-stabilized burner along the jet-flame centreline. The signal to noise ratio was circa 60. The local temperature distribution was affected by the swirl numbers and downstream positions. The presence of the recirculation zone resulted in higher downstream mean temperatures for higher swirl numbers 1.07. On the contrary, for the lowest swirl number of 0.3 the flame behaved more like a jet flame with low mean downstream temperatures. The flame was stably attached to the fuel nozzle for all three swirl numbers. The flame seemed to be stabilized by the recirculation of hot gases because no combustion could be sustained when no swirling component was used for the same total flow rate. Temperature spectra demonstrated relatively short inertial subrange for low swirl number and extended subrange for higher ones.

6. Acknowledgment

7. Nomenclature

S – Swirl number

G_θ – Axial flux of angular momentum

G_z – Axial flux of axial momentum

D – Burner internal diameter (coflow pipe)

ρ – Air density

U – Axial velocity

W_r – Tangential velocity

R – Burner radius (D/2)

T – Flame temperature

T_{ref} – Reference temperature

S_{ref} – Reference signal at known T_{ref}

S_{meas} – Measured Rayleigh signal at unknown T

8. References

1. A.K. Gupta, D.G. Lilley, and N. Syred. Swirl flows. ABACUS Press, Cambridge, USA, 1985.

2. W. Steenbergen. Turbulent pipe flow with swirl (PhD thesis). Technishe Universiteit Eindhoven, Netherlands, 1995.

3. G. Bulat. Large Eddy Simulations of Reacting Swirling Flows in an Industrial Burner (PhD thesis). Department of Mechanical Engineering Imperial College London, UK, 2012.

4. R. Orlu. Experimental study of passive scalar mixing in swirling jet flows. Technical Reports from Royal Institute of Technology KTH Mechanics, Stockholm, Sweden, 2006.

5. Y. Huang. Combustion dynamics of swirl-stabilized lean premixed flames in an acoustically-driven environment (PhD thesis). University of Iowa, 2008.

6. A.F. Moene. Swirling pipe flow with axial strain Experiment and Large Eddy Simulation (PhD thesis). Technische Universiteit Eindhoven, 2003.

7. Y. Hardalupas, N. Soulopoulos, V. Stetsyuk and Alex M. K. P. Taylor. Experimental Assessment of 'subgrid' scale Probability Density Function Models for Large Eddy Simulation. 16th Int. Symp. on Applications of Laser Techniques to Fluid Mechanics, Lisbon, Portugal, 09-12 July, 2012.

8. T.F. Dixon, J. S. Truelove and T. F. Wall. Aerodynamic studies on swirled coaxial jets from nozzles with divergent quarls. J. of Fluids Eng., Vol 105, pp.197-203, 1983.

9. V.D. Milosavljevic. Natural gas, kerosene and pulverized fuel fired swirl burners. (PhD thesis), Imperial College of Science Technology and Medicine. Department of Mechanical Engineering. 1993.

10. R. Cabra, T. Myhrvold, J.Y. Chen, and R.W. Dibble. Simultaneous Laser Raman-Rayleigh-LIF Measurements and Numerical Modeling Results of a Lifted Turbulent H2/N2 Jet Flame in a Vitiated Coflow. 29th International Symposium on Combustion, Sapporo, Japan, July 21-26, 2002.

11. A.M.K.P. Taylor (ed). Instrumentation for flows with combustion. Academic press limited, 1993.